

Testing gravitational redshift based on microwave frequency links onboard the China Space Station

Wenbin Shen,^{1,2,3,*} Pengfei Zhang^{1,2}, Ziyu Shen,^{4,†} Rui Xu^{1,2}, Xiao Sun,³ Mostafa Ashry^{1,2,3,5}, Abdelrahim Ruby^{1,2,3}, Wei Xu,^{1,2} Kuangchao Wu,^{1,2} Yifan Wu,^{1,2} An Ning,^{1,2} Lei Wang,^{1,2} Lihong Li,^{1,2} and Chenghui Cai^{1,2}

¹*School of Geodesy and Geomatics, Wuhan University, Wuhan 430079, China*

²*Time and Frequency Geodesy Center, Wuhan University, Wuhan 430079, China*

³*State Key Laboratory of Information Engineering in Surveying, Mapping and Remote Sensing, Wuhan University, Wuhan 430079, China*

⁴*School of Resource, Environmental Science and Engineering,*

Hubei University of Science and Technology, Xianning, Hubei, China

⁵*Civil Engineering Department, Faculty of Engineering, Minia University, Minia 61111, Egypt*



(Received 7 December 2021; accepted 27 June 2023; published 15 September 2023; corrected 26 October 2023)

In November 2022, the China Space Station (CSS) was equipped with a cold atomic microwave clock and a Sr optical lattice clock with stabilities of $5 \times 10^{-14}/\sqrt{\tau}$ and $2 \times 10^{-15}/\sqrt{\tau}$ (where τ is the integration time in seconds), respectively, which provides an excellent opportunity to test gravitational redshift (GRS) with higher accuracy than previous results. Based on high-precision frequency links between the China Space Station and a ground station, we formulated a model and provided simulation experiments to test GRS. Simulation results suggest that this method could test the GRS at the accuracy level of 5×10^{-7} , more than 2 orders in magnitude higher than the result of the experiment of a hydrogen clock on board a flying rocket more than 40 years ago.

DOI: [10.1103/PhysRevD.108.064031](https://doi.org/10.1103/PhysRevD.108.064031)

I. INTRODUCTION

Scientists paid great attention to testing the gravitational redshift (GRS) effect, one of three classic predictions of general relativity theory (GRT). In 1976 scientists conducted the Gravity Probe-A (GP-A) experiment mission to test GRS [1]. A hydrogen atomic clock was on board a rocket in this mission, which flew about two hours in space. Based on the microwave links between the rocket and several ground stations, the GP-A experiment has tested the relativistic frequency shift at the accuracy level of 7×10^{-5} . To improve the accuracy level, one should consider two aspects. In one aspect, we try to use better clocks with higher stability and accuracy. In another aspect, we try to create a condition that the gravitational potential difference between two points is as significant as possible. For instance, using optic clocks with stabilities around 10^{-18} , Katori's group [2] measured a height of 450 m with an accuracy of 4.1 cm, by which the accuracy of testing GRS achieves 9.1×10^{-5} , a little worse than the previous rocket-experiment result of 7×10^{-5} [3]. Another example, based on observations from two eccentric-orbit Galileo satellites, E14 and E18 (the stabilities of the onboard clocks are around $10^{-15}/\text{day}$), several groups tested GRS with an accuracy level around $2.5\text{--}4.5 \times 10^{-5}$ [4–6].

Recently, a few space atomic clock projects have been put forward, for example, the Atomic Clock Ensemble in Space (ACES) mission onboard the international space station (ISS) and the China Space Station (CSS) mission. The ACES mission will be equipped with an atomic clock with long-term stability 2×10^{-16} [7,8], and use its two independent time and frequency transfer links, including three microwave links (MWL) and two European Laser Timing optical links to distribute time and frequency scale to the ground stations. By using one uplink and two downlinks MWL, a trifrequency combination method for time-frequency transfer is constructed according to the accuracy of the ACES atomic clock [9,10]. Verified by simulation experiments, the trifrequency combination method may test GRS at a level of 10^{-6} [11,12]. The CSS and ACES are different in design. The CSS has been equipped with a Sr optical lattice clock with a stability of $2 \times 10^{-15}/\sqrt{\tau}$ [11–15] (τ is given in seconds), and two up-microwave links from a ground station to CSS and two down-microwave links from CSS to the ground station will be established. One uplink signal and one downlink signal have the same frequency of 30.4 GHz but different circular polarization directions. Considering the MWL characters, most kinds of errors caused by the propagation will be eliminated. This study created a new frequency transfer model used in the space-ground frequency transfer to test GRS, which is at least an order of magnitude higher than the results given by previous studies.

*2891983829@qq.com

†theorhythm@foxmail.com

This paper is organized as follows. Section I introduces the relevant background of GRS and atomic clock projects. Section II presents the CSS and its high-precision time and frequency systems. In Sec. III, under the frame of general relativity, we formulated a model for frequency transfer that is accurate to the order c^{-4} . Section IV describes the simulation experiments of testing GRS. Finally, we conclude this work in the last section.

II. CHINA SPACE STATION

The CSS designed three modules, one core module (CM) and two experiments modules (EM). The CSS has been launched to an orbit with a height of around 400 km above the ground since April 29, 2021. From June 17 to September 16, 2021, three Chinese astronauts stayed in the TianHe core module of the CSS to prepare for future experiments. Since October 16, another three Chinese astronauts have been successively launched in the core module for further preparatory work.

The CSS will stay in orbit for at least ten years. For the purpose of time and frequency applications, the CSS has established a high-precision time and frequency system (HPTFS) consisting of a set of clocks (See Fig. 1). Three or more ground stations have been or will be established,

including, for instance, Beijing, Xi'An, Shanghai, and Wuhan stations. Additionally, a mobile observation station will be established for time and frequency comparisons for more general and prospective applications. In addition, the space-ground signals links between CSS and ground stations, including MWL and laser links, will be established. It is noted that, as planned by the CSS project, the MWLs and the laser links will work officially and normally, starting from May 2023. In this section, we will introduce the HPTFS and MWL, respectively.

A. High-precision time and frequency system

The CSS is designed as a T-shape configuration, and the experiments module II (EM II) had been launched and attached to the core module in the first week of November 2022. It is equipped with HPTFS, which contains a Sr optical lattice clock, an active hydrogen maser, and a cold atom microwave clock.

As Fig. 1 shows, the HPTFS occupies 2 cabinets of the EM II. One cabinet is for the Sr optical lattice clock system, which consists of a vacuum cavity, the optical and electronic parts of the clock, narrow line laser, frequency penetration and transfer unit, and a FOFC. Another cabinet contains an active hydrogen maser, an Rb atom microwave clock, FCDS, and the precision orbit determination unit,

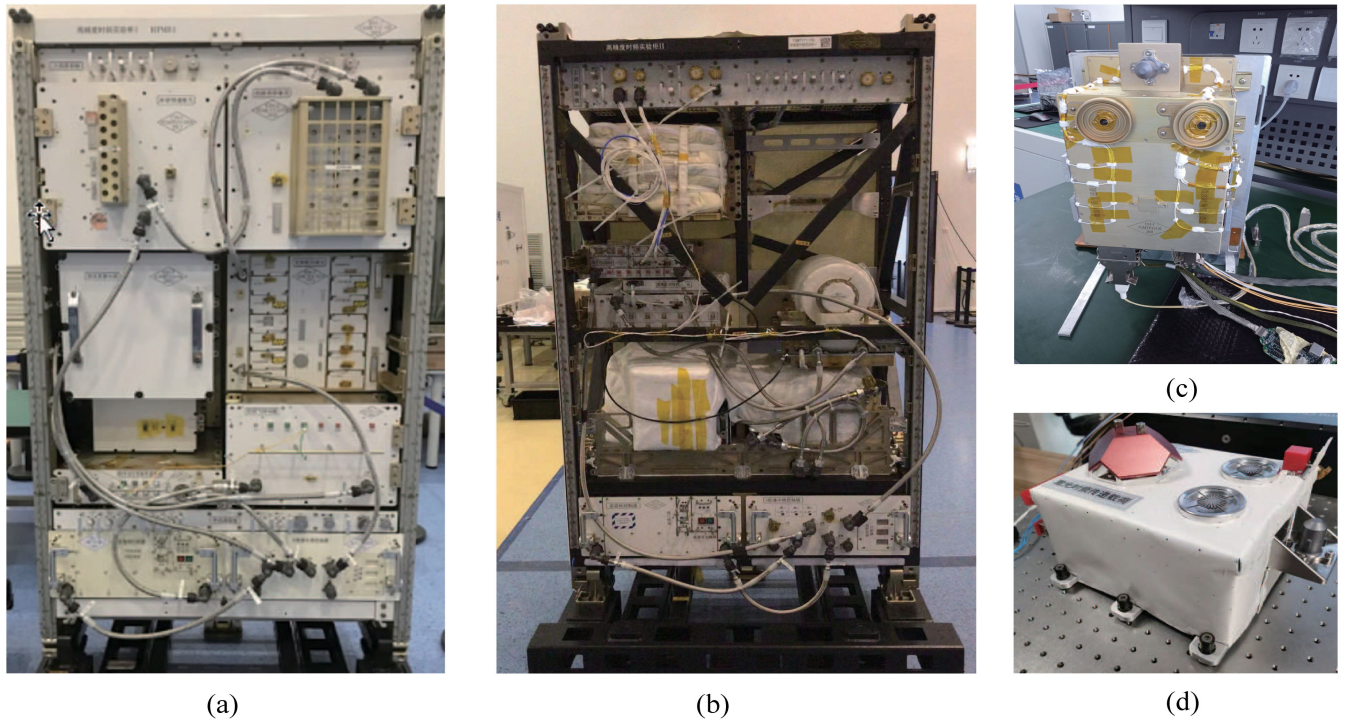


FIG. 1. High-precision time and frequency system (modified after [16]). (a) In this cabinet there is a Sr optical lattice clock, consisting of (from left to right and from top to bottom in order) a vacuum cavity, the optical part, the narrow-line laser, the electronic part, the frequency penetration and transfer unit, and the femtosecond optical frequency comb (FOFC). (b) In the second cabinet there is a cold atom microwave clock, an active hydrogen clock, a precision orbit determination unit, and the frequency comparison and distribution system (FCDS). (c) The payload of microwave signals emitting and receiving equipment. (d) The payload of laser time-frequency transfer.

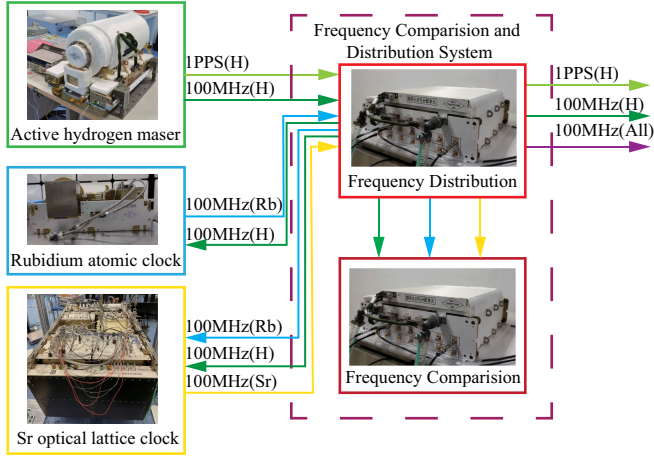


FIG. 2. Major core equipment and signals of high-precision time and frequency system (modified after [17]). The active hydrogen maser provides 1 PPS signal and 100 MHz frequency signal with the stability of $2 \times 10^{-13}/\sqrt{\tau}$. The Rb atom microwave clock and Sr optical lattice clock provide 100 MHz frequency signals with the stabilities $5 \times 10^{-14}/\sqrt{\tau}$ and $2 \times 10^{-15}/\sqrt{\tau}$, respectively. The FCDS mainly makes frequency comparison and combination and signals distribution.

which can use the global navigation satellite system (GNSS) to measure the CSS instantaneous position [See Fig. 1(b)]. Figures 1(c) and 1(d) show, respectively, the microwave and laser time and frequency transfer outside the CSS. The payload of microwave time and frequency transfer has two antennas, one is used to receive microwave signals from the ground stations, and another one is used to emit microwave signals to the ground.

Figure 2 shows the working process of the HPTFS. The hydrogen maser outputs one 1 Pulse Per Second (PPS) signal to the FCDS. Every clock outputs one 100 MHz signal to the FCDS, then the FCDS distributes the 100 MHz signals of the hydrogen maser to the microwave clock and optical clock as a long-term frequency reference. The daily stability of the hydrogen maser and microwave clock may reach 2×10^{-15} and 2×10^{-16} , respectively [15]. The optical clock stability could achieve $2 \times 10^{-15}/\sqrt{\tau}$ [12,15]. These three 100 MHz of different clocks make the frequency comparison by the FCDS and output one 100 MHz signal to FOFC [see Fig. 1(a)]. 1 PPS and 100 MHz signals from the hydrogen maser were also sent to the FOFC by FCDS. Through the frequency penetration and transfer unit, signals reach the time and frequency transfer payload of microwave and laser. They will emit the microwave and laser signals to the ground stations.

B. Microwave links

There will be four MWLs between CSS and a ground station of interest for time and frequency transfer. The MWLs consist of two uplinks and two downlinks as listed in Table I. Compared with the ACES mission, there are two

TABLE I. Parameters of the CSS and frequency links.

Parameter	Value
Altitude	~ 400 km
Uplink frequency	30.4 GHz, 26.8 GHz (both left-hand circularly polarized)
Downlink frequency	30.4 GHz, 20.8 GHz (both right-hand circularly polarized)
Orbit inclination	41.5°
Minimum visible elevation angle	5°
Observation cutoff elevation angle	15°

changes: One is that the CSS mission has an additional uplink with its frequency equal to one, the downlink signal frequency. Another is that the one uplink and one downlink signals are left-hand and right-hand circularly polarized, respectively. In ACES, there are three microwave signals all with the left-hand polarization direction, one uplink (Ku-band, 13.475 GHz), and two downlinks with frequencies 2.248 GHz and 14.703 GHz, respectively [18]. This setup makes it easy for the receiver to distinguish between uplinks and downlinks [18]. While the CSS payload will use the same frequency signal at the same time, the receiving antenna not only receives the useful signal from the remote end but also receives interference signals from the emitting antenna. The power of the self-interfering signal is much larger than that of the signal with the proper reception of useful signals [19]. To separate the signal of interest from the interfering signals, the CSS mission uses the Co-time Co-frequency Full Duplex technology, which effectively realizes self-interference cancellation [20,21]. Scientists often make self-interference suppression in the airspace, radio frequency (RF) domain, and digital domain. The MWL system is designed with a three-stage interference cancellation scheme, which includes three parts: antenna isolation cancellation, RF cancellation, and digital baseband cancellation [16]. The simplest self-interference cancellation mechanism is antenna separation. In the free space, the microwave signal transmission loss is $L = 32.45 + 20 \log_{10}(f) + 20 \log_{10}(d)$ [22,23], where f is frequency in megahertz, and d is the distance in kilometers. Hence, when the microwave (radio) frequency f is given, the transmission loss increases with the increase of the distance between the CSS and ground station, and in addition, the self-interference cancellation becomes better with larger antenna separation (because the influence becomes weaker). In practice, with the limited CSS space, the distance between the two antennas is also limited, but the distance must be large enough to distinguish the emitted and received radio frequency signals. As Fig. 1(c) shows, the emitting and receiving antennas both on board the CSS and ground station are separated to achieve high isolation performance through the effective suppression of space

and surface waves [24]. The gains of the CSS antenna and ground station antenna are -5 dB and 54.7 dB for 30.4 GHz respectively. The effective isotropic radiated power (EIRP) of the CSS antenna is -5 dBm [16]. In the CSS, it uses the following technique: the “antenna separation cancellation + RF cancellation + baseband digital cancellation” (simply three-stage self-interference) technique is used to make the self-interference cancellation. The ground test shows the three-stage self-interference cancellation technique is sufficient to effectively distinguish the up and down signals when the two antenna distance is 10 cm [16,24]. The test on the ground shows the antenna separation technology can achieve approximately 60 dB of cancellation [16]. The multipath reflection energy of the transmitted signals is cancelled by coupling out of the reference signal into the offset RF network, and the RF cancellation is about 10 dB [16,25,26]. By using the broadband spread code signal, analog-to-digital converter effective quantization bits are close to 10 bits and the digital interference cancellation capacity reaches the upper limit of about 45 dB [16,27]. By self-interference cancellation, the MWL system’s total interference cancellation capability reaches 115 dB, which can identify up and down links with the same frequency but with opposite polarization directions (left-hand circularly polarized uplink signal and right-hand circularly polarized downlink signal).

When passing through the atmosphere, the signals will be affected by the troposphere and ionosphere. In addition, the relative motion between the CSS and the ground station gives rise to the Doppler effect. These influences will cause additional frequency shifts besides the gravitational frequency shifts. Here in this study, we use only up- and downlink signals both with frequency 30.4 GHz (see

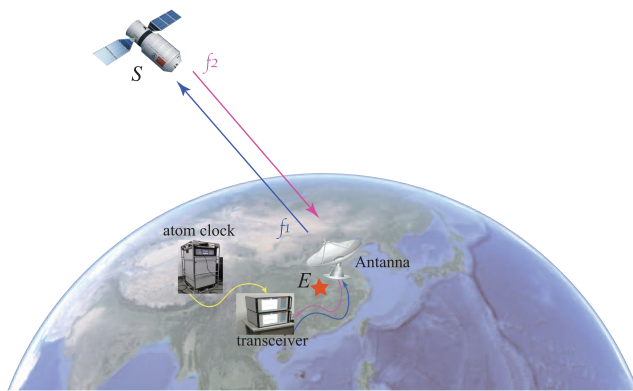


FIG. 3. One uplink and one downlink of microwave signals between the CSS noted as S and a ground station (E) at Wuhan, China. The uplink (f_1) and downlink (f_2) are, respectively, left- and right-hand circularly polarized signals both with the frequency 30.4 GHz. The antenna and the atomic clock at the ground station are linked by a transceiver. The received signals from the CSS are compared with the local signals generated by the ground clock.

Fig. 3), and the other two links with different frequencies (see Table I) will not be used. Since the frequencies of the uplink and downlink are the same, the uninteresting frequency shifts caused by the first-order Doppler effects, troposphere effects, and ionosphere effects are similar. Making a difference between the up and downlinks, we may cancel the uninterested frequency shifts and double the GRS, which provides an opportunity to test GR with higher accuracy.

III. FORMULATION OF FREQUENCY TRANSFER MODEL

A. Methodology

To be comparable with the stability of the optical clocks, the one-way frequency transfer model to the order c^{-4} is established, which guarantees the model accuracy being better than 10^{-18} [10].

The up-link and down-link signals between the CSS (denoted as S) and ground station (denoted as E) satisfy the following expression:

$$\begin{aligned} f_{IJ}^r &= f_{IJ}^e - \Delta U_{IJ}f + \Delta f_{\text{Dop1-}IJ} + \Delta f_{\text{Dop2-}IJ} \\ &+ \Delta f_{\text{tro-}IJ} + (\Delta f_{\text{ion1-}IJ} + \Delta f_{\text{ion2-}IJ}) \\ &- \Delta f_{\text{ti-}IJ} - \Delta f_{\text{pl-}IJ} + \epsilon_{IJ} \end{aligned} \quad (1)$$

where $I, J = E, S, I \neq J$, E and S denote Earth and space station, respectively; f_{IJ}^r is the received frequency of the signal at J coming from I , f_{IJ}^e is the emitting frequency of the signal at I toward J ; $\Delta U_{IJ} = U_J - U_I$, U_I is the Earth’s gravitational potential at I , f is the nominal frequency (30.4 GHz), $\Delta f_{\text{Dop1-}IJ}$ and $\Delta f_{\text{Dop2-}IJ}$ are the first- and second-order Doppler frequency shifts of the signals transmitting from I to J , $\Delta f_{\text{tro-}IJ}$ is the frequency shift of the signal transmitting from I to J caused by the troposphere, $\Delta f_{\text{ion1-}IJ}$ and $\Delta f_{\text{ion2-}IJ}$ are the first- and second-order frequency shifts of the signal transmitting from I to J caused by the ionosphere, $\Delta f_{\text{ti-}IJ}$ and $\Delta f_{\text{pl-}IJ}$ are frequency shifts caused by tides and external celestial bodies (including the sun, moon, Mercury, Venus, Mars, Jupiter, etc.), respectively, and ϵ_{IJ} are the higher-order terms that are calculated based on proper models [9–12] and the unmodeled errors of the signals transmitting from I to J , including for instance the clock errors, random errors, and other noises. As presently designed in the CSS, the uplink signal with frequency $f_1 = 30.4$ GHz is left-hand circularly polarized, and the downlink signal with frequency $f_2 = 30.4$ GHz is right-hand circularly polarized [13,14]. In an ideal situation, the uplink and downlink signals are emitted at the same time. Regardless of the signal’s propagation time, we have $\Delta f_{\text{ion2-}ES} = \Delta f_{\text{ion2-}SE}$ [28]. In addition, taking into account the following relationships: $\Delta U_{IJ} = -\Delta U_{JI}$, $\Delta f_{\text{Dop1-}IJ} = \Delta f_{\text{Dop1-}JI}$, $\Delta f_{\text{tro-}IJ} = \Delta f_{\text{tro-}JI}$, $\Delta f_{\text{ion1-}IJ} = \Delta f_{\text{ion1-}JI}$, $\Delta f_{\text{ti-}IJ} = -\Delta f_{\text{ti-}JI}$, and

$\Delta f_{pl-IJ} = -\Delta f_{pl-JI}$, from Eq. (1), subtracting f_{ES}^r from f_{SE}^r , we obtain

$$\Delta U_{SE} = \frac{1}{f} \left(\frac{f_{SE}^r - f_{ES}^r}{2} + \frac{f_{\text{Dop}_{2-SE}} - f_{\text{Dop}_{2-ES}}}{2} - \Delta f_{ii-SE} - \Delta f_{pl-SE} + \varepsilon \right) \quad (2)$$

where $\varepsilon = -(\varepsilon_{SE} - \varepsilon_{ES})/2$. However, due to the movements of the CSS and the ground station, the paths of the up- and down-signals are different, which leads to a path discrepancy. Hence, Eq. (2) may be modified as

$$\Delta U_{SE} = \frac{1}{f} \left(\frac{f_{SE}^r - f_{ES}^r}{2} + \frac{f_{\text{Dop}_{2-SE}} - f_{\text{Dop}_{2-ES}}}{2} - \Delta f_{ii-SE} - \Delta f_{pl-SE} + \Delta f_p + \varepsilon \right) \quad (3)$$

where Δf_p is the path discrepancy frequency shift. On the right-hand side of Eq. (3), the first term is directly observed, the second term is the second Doppler effect, and the third and fourth terms, Δf_{ii-SE} and Δf_{pl-SE} , can be calculated by relevant models. For instance, the tides can be corrected by the tide model [29–31], and general formulas can directly correct the influences by external celestial bodies [32,33]. In Eq. (3), both the first- and second-order ionospheric frequency shifts vanish because one left-hand (uplink) and another right-hand (downlink) circularly polarized wave signal are designed in CSS. In practice, the uplink signal's path does not coincide with the downlink signal's path. After the combination of the up and down frequency signals, there are still the following residual errors: path discrepancy frequency shifts (including first- and second-Doppler effects), and troposphere and ionosphere frequency shift residuals as shown in Table III.

At a given time t , we can obtain an observation of ΔU_{ES} . Comparing the observation with the corresponding true (model) value ΔV_{ES} , we can get the offset between the observed value and the model value, expressed in relative difference as

$$\alpha = \frac{\Delta U(t)_{ES} - \Delta V(t)_{ES}}{V(t)_{ES}} \quad (4)$$

which describes the deviation of the observed result based on GRT from the true (model) value. If GRT holds, $\alpha = 0$.

For convenience, the formulation described in this section is referred to as the two frequency combination (TFC) technique.

B. Error sources

When a MWL passes through the atmosphere from the CSS to the ground station or reversed, there are several kinds of errors, including orbit and velocity determination errors, which give rise to the main errors of Doppler

frequency shifts, atmosphere (ionosphere and troposphere) effects, solid earth tidal effects, and other undefined errors. We need to study the different error models and eliminate their influences.

1. Doppler effects

The Doppler effects are the main errors in the MWL time and frequency transmission process, which must be eliminated. The Doppler effects are caused by the CSS relative motion to the ground stations when it approaches and moves away from them. The first-order and second-order Doppler effects can be expressed as [10]

$$\Delta f_{\text{Dop}_{1-IJ}} = -\frac{f}{c} \mathbf{N}_{IJ} \cdot (\mathbf{v}_I - \mathbf{v}_J) \quad (5)$$

$$\Delta f_{\text{Dop}_{2-IJ}} = \frac{f}{c^2} \left\{ \frac{v_I^2}{2} - \frac{v_J^2}{2} - [\mathbf{N}_{IJ} \cdot (\mathbf{v}_I - \mathbf{v}_J)] (\mathbf{N}_{IJ} \cdot \mathbf{v}_J) \right\} \quad (6)$$

where c is the velocity of light in vacuum, I and J have the same meaning as explained after Eq. (1), \mathbf{N}_{IJ} is the unit vector from I to J , and \mathbf{v}_I and \mathbf{v}_J are the velocities of I and J , respectively. From Eq. (5), we find the first-order Doppler effects of the up- and downlinks hold the same and they can be eliminated by the difference between the up- and downlinks except for the residual errors due to the discrepancy between the uplink and downlink paths, which are further corrected. Equation (6) shows the second-order Doppler effect, which is about 5–6 orders smaller than the first-order Doppler effect. The first-order Doppler residual and the second-order Doppler effect are corrected by the given positions and velocities of the CSS and ground stations. As shown in Fig. 1, the HTFS is equipped with a precision orbit determination unit [See Fig. 1(b)], which provides the positions and velocities of the CSS.

2. Clock error

Many scholars have worked on the time and frequency stability characteristic and assumed that the average output of an oscillator is a voltage which is expressed as [34]

$$V(t) = [V_0 + \varepsilon(t)] \sin [2\pi v_0 t + \varphi(t)] \quad (7)$$

where V_0 denotes the nominal amplitude and v_0 is the nominal frequency, respectively. $\varepsilon(t)$ is the deviation of amplitude from nominal and $\varphi(t)$ represent phase deviations [35].

The instantaneous output frequency of the atomic clock is defined as [34,35]

$$v(t) = v_0 + \frac{1}{2\pi} \frac{d\varphi(t)}{dt}. \quad (8)$$

In a stable frequency generator, the fractional frequency fluctuation can be derived from Eq. (8) as $y(t) = \dot{\varphi}(t)/2\pi v_0$.

We assume $y(t)$ is a random function of time, and the mean value equals zero. The one-sided power spectra density of the $y(t)$ can be expressed as [34,36]

$$S_y(f_F) = \sum_{\beta=-2}^2 h_\beta (f_F)^\beta \quad (9)$$

where h_β is the noise intensity coefficient of the energy spectrum with noise index $\beta = -2, -1, 0, 1, 2$, and f_F is the Fourier frequency variable.

The atomic clock noises are complex and classified as five different types of stochastic noises, which correspond to the different values of β . The white phase modulation noise ($\beta = 2$) is the result of the quantum (for optical frequencies) noise [37]. The flicker phase modulation noise ($\beta = 1$) is mainly generated in transistors. The white frequency modulation noise ($\beta = 0$) is often masked by other types of noise. It is determined by the oscillator bandwidth white noise and observed in lasers and masers [38,39]. The flicker frequency modulation noise ($\beta = -1$) and random walk frequency modulation noise ($\beta = -2$) might be connected with the photon energy density and limit the long-term frequency stability of the atomic clock [37].

3. Ionospheric and tropospheric frequency shifts

The MWL signal is influenced by the atmosphere during its propagation. There are some frequency shifts Δf caused by the atmosphere (including ionosphere and troposphere) [40]:

$$\Delta f = -\frac{f}{c} \frac{dP}{dt} \quad (10)$$

where $P = \int_L n dl$ is the phase path in the atmosphere, n is the refractive index of the atmosphere, and L is the signal's propagation path through the atmosphere. Substituting the expression of P into Eq. (10) and removing the conventional first-order Doppler shifts, we can deduce the atmospheric frequency shifts [12,40–42]:

$$\begin{aligned} \Delta f_{atm} &= -\frac{f}{c} \frac{d}{dt} \int_L (n-1) dl \\ &= -\frac{f}{c} \frac{d}{dt} \int_{L_i} (n_i-1) dl_i - \frac{f}{c} \frac{d}{dt} \int_{L_t} (n_t-1) dl_t \end{aligned} \quad (11)$$

where L_i and L_t are the signal's propagation paths through the ionosphere and troposphere, n_i and n_t are the ionospheric and tropospheric refractive indexes, respectively, and dl_i and dl_t are integral elements along the corresponding paths, respectively. The first term on the right-hand side of Eq. (11) is the ionospheric frequency shift Δf_{ion} , and the second term is the tropospheric frequency shift Δf_{tro} .

In order to calculate the ionospheric and tropospheric frequency shifts, the refractive indexes, n_i and n_t , need to be determined. From the previous studies, the ionospheric refractive index accurate to f^{-4} is [28,43]

$$n_i = 1 - 40.3 \frac{N_e}{f^2} \pm \frac{7527 \times c}{2f^3} N_e B_0 \cos \theta - \frac{812.3}{f^4} N_e^2 \quad (12)$$

where N_e is the electron density per m^3 , B_0 is the strength of the geomagnetic field, and θ is the angle between the wave propagation direction and the geomagnetic field vector. The positive sign (+) and negative sign (−) represent the left- and right-hand circularly polarized MWLs, respectively [43].

The tropospheric refractive index n_t is estimated as [12,44]

$$n_t = 1 + \left(k_1 \frac{p_d}{T} + k_2 \frac{p_w}{T} + k_3 \frac{p_w}{T^2} \right) \times 10^{-6} \quad (13)$$

where T is the temperature in Kelvin, p_d and p_w represent the dry air and water vapor partial pressures respectively, the constants $k_1 = 77.6890$, $k_2 = 71.2952$, and $k_3 = 375463$.

The ionospheric and tropospheric frequency shifts can be obtained by substituting Eqs. (12) and (13) into Eq. (11), respectively. Then, we have

$$\begin{aligned} \Delta f_{ion} &= 40.3 \frac{1}{c} \frac{d}{dt} \int_{L_i} N_e dl_i \\ &\mp \frac{7527}{2f^2} \frac{d}{dt} \int_{L_i} N_e B_0 \cos \theta dl_i + \frac{812.3}{cf^3} \frac{d}{dt} \int_{L_i} N_e^2 dl_i. \end{aligned} \quad (14)$$

In Eq. (14), the first- and third-order terms are relative to the electron density and not related to the microwave polarization direction, and they hold the same for the up- and downlinks. For the second-order term, the up- and downlinks have different polarization directions; the signs are reversed. However, since the angles between the wave propagation direction and the geomagnetic field vector of the up- and downlinks are θ_u and θ_d , respectively, $\theta_u + \theta_d \approx 180^\circ$, the second-order frequency shifts for the up- and downlinks hold also same.

Similarly, we have

$$\Delta f_{tro} = -\frac{f}{c} \frac{d}{dt} \int_{L_t} \left(k_1 \frac{p_d}{T} + k_2 \frac{p_w}{T} + k_3 \frac{p_w}{T^2} \right) \times 10^{-6} dl_t \quad (15)$$

From Eq. (15), the tropospheric frequency shifts have the same values for up- and downlinks, which are independent of the microwave polarization direction. In practice, we use the Saastamoinen model [45] and Vienna mapping function (VMF) [46] to calculate the tropospheric propagation effect, which is extensively used in GNSS positioning, and then take the derivative of time to obtain the tropospheric frequency shifts.

4. Earth tides

The deformation of the Earth will cause potential changes outside the Earth's surface. The tidal displacements include solid Earth tides, ocean tides, and polar tides.

$$\Delta V(r, \phi, \lambda) = \frac{GM}{r} \sum_{n=0}^N \left(\frac{R_e}{r}\right)^n \sum_{m=0}^n [\Delta \bar{C}_{nm} \cos(m\lambda) + \Delta \bar{S}_{nm} \sin(m\lambda)] \bar{P}_{nm}(\sin \phi) \quad (16)$$

where r is the distance from the geocenter to the field point, ϕ and λ represent the latitude and longitude of the field point, GM and R_e denote the gravitational parameter and the equatorial radius of the Earth, respectively, \bar{P}_{nm} are the normalized associated Legendre functions, and $\Delta \bar{C}_{nm}$ and $\Delta \bar{S}_{nm}$ are the changes of normalized geopotential coefficients which due to Earth tides. They can be expressed by terms of the Love number k . The detailed calculation processes are referred to as International Earth Rotation and Reference Systems Service (IERS) Conventions 2010 [29].

5. Other error sources

Besides the mentioned errors, there are other error sources, mainly including the Shapiro effect and path discrepancy. The magnitudes of the errors and the magnitudes of the residual errors after TFC or TFC/model corrections are listed in Table II. According to Eqs. (1) and (3), the first-order Doppler effect, ionospheric frequency shifts, and tropospheric frequency shifts can be eliminated by making a difference between the uplink and downlink. However, the tide effect remains as big as previously. The path discrepancy effect contains the residuals of the ionosphere, troposphere, and first-order Doppler effects after the TFC technique. The residual error of the first-order Doppler effect after a TFC caused by path discrepancy is about 5.7×10^{-18} . After TFC, the ionospheric and tropospheric frequency shift residuals are about 7.6×10^{-18} and 1.1×10^{-16} , respectively, and after further models corrections, the residuals could be reduced to 7.6×10^{-19} and 5.3×10^{-17} , respectively. As the tide effect can not be eliminated by the TFC, they are corrected by the

Solid Earth tides are the main influence, which leads to displacements of about tens of centimeters per day [29]. The tidal potential ΔV can be described by a spherical harmonics of N degree as [29]

tide model mentioned in Sec. III B 4. The total residual error is less than 5.3×10^{-17} .

IV. SIMULATION EXPERIMENTS

In our simulation experiments, we chose Luojia time and frequency station (LTFS) at Wuhan as the ground station, the coordinates of which are ($30^{\circ}31'51.90274''$ N, $114^{\circ}21'25.83516''$ E, 25.728 m). The CSS parameters and signals' original emitted frequency values are shown in Table I. The observations in our simulation experiments are the received frequency signals between the ground station LTFS and the CSS, denoted as f_{IJ}^r , which includes various frequency shifts caused by different factors, as expressed by Eq. (1). When we make the simulation experiment, the first-order Doppler frequency shifts, relativistic frequency shifts (including gravitational redshift and second-order Doppler effect), atmospheric frequency shift, tidal frequency shift, and clock noises are calculated by the different models in Sec. III to obtain the received frequency values.

In the simulation experiments, we first calculate the CSS and ground station positions and velocities. The two-line element sets (TLEs) are a special term used in the orbit of a spacecraft field, and it is defined in detail in NORAD. The TLEs provide not only six Keplerian elements, including the inclination of the orbits, right ascension of the ascending node, eccentricity, argument of perigee, mean anomaly, and mean motion, but also other information about the spacecraft [47]. We obtain the TLEs of the CSS from the North American Aerospace Defense Command (NORAD) website [48]. Using the relevant parameters can calculate

TABLE II. The magnitudes of different error sources and residual errors.

Error sources	Magnitudes of errors	Magnitudes of residual errors	Method
Shapiro effect	$\sim 3 \times 10^{-14}$	$\sim 10^{-22}$	TFC ^a
Tropospheric effect	$\sim 3 \times 10^{-10}$	$< 5.3 \times 10^{-17}$	TFC + trop model
Ionospheric effect	$\sim 6.0 \times 10^{-13}$	$< 7.6 \times 10^{-19}$	TFC + iono model
First-order Doppler effect	$\sim 10^{-5} - 10^{-6}$	$< 5.7 \times 10^{-18}$	TFC
Tide effect for CSS	$< 1.7 \times 10^{-17}$	$< 2 \times 10^{-18}$	Tide model
Tide effect for Ground Station	$< 1.5 \times 10^{-17}$	$< 2 \times 10^{-18}$	Tide model
Total frequency shift	$10^{-5} \sim 10^{-6}$	$< 5.3 \times 10^{-17}$...

^aTwo frequency combination (TFC).

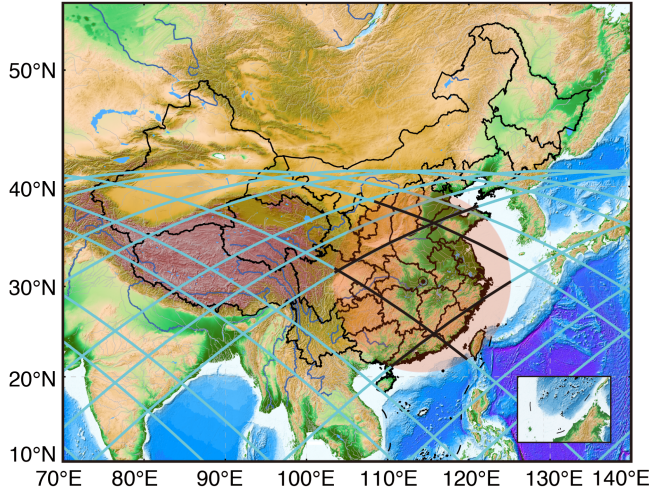


FIG. 4. The orbit of the CSS in Earth centered Earth fixed coordinates during the observations in one day. The ground station is located in Wuhan, China ($30^{\circ}31'51.90274''$ N, $114^{\circ}21'25.83516''$ E, 25.728 m). The observation period is from June 1, 00:00 to June 2, 00:00, 2021. The light-colored lines denote when the CSS and Wuhan station are not intervisible. The solid black lines denote when the CSS and Wuhan station are intervisible and observation values are available.

the CSS orbit positions and velocities, which are assumed as real values. From the “China Space Station science experiment resource manual,” the position and velocity accuracy are designed as 10 cm and 1 mm/s [15], respectively. To obtain a better result, we set the observation cutoff elevation angle of the CSS larger than 15° .

The clock error model [Eq. (8)] is used to simulate the CSS and ground clock errors. To obtain the atmospheric effects on the frequency, we use the Saastamoinen model [45] and the VMF [46] to generate the atmospheric frequency shifts. The meteorological parameters in the space region near and around the LTFS are downloaded from the CDDIS (Crustal Dynamics Data Information System) website [49]. To simulate the ionospheric frequency shift, we need the electron density and geomagnetic strength data. Here, we use the International Reference Ionosphere model [50] and the international geomagnetic reference field model [51] to obtain the relevant data to

simulate the first- and second-order ionospheric frequency shifts. We use the IERS Convention 2010 [29] to calculate the tidal harmonic parameters and use the NASA software SPICE [52] to calculate the tidal forcing for a given time.

According to the simulation setup, we may obtain the observed values f_{IJ}^r based on emitting frequency values. By Eq. (2), the value of ΔU_{SE} could be calculated. We use the EGM2008 model [53] to calculate the gravitational potentials at the CSS and ground station to obtain ΔV_{ES} as the true value.

We have conducted simulation experiments to estimate the feasibility of a GRS test based on the CSS. The experiment lasts one day, from June 1, 00:00 to June 2, 00:00, 2021. The orbit simulated data were generated by TLEs [47], which is used to describe a spacecraft orbit and to predict its position and velocity. The trace of the CSS during one day was depicted in Fig. 4. Figure 4 shows that the ground station can observe the CSS about 4 or 5 times daily. When the CSS passed the ground station, we can only observe the MWLs for about 300 s. The total observation time is about 20 minutes in one day. In the subsequent simulation experiment, we take one-day records as one observation dataset, and the total observation times are 40 days. For 40 days of simulation experiment, the total time was around 86400 s. The gravitational potential at the space station was calculated by EGM2008 [54]. The precision of EGM2008 is about several centimeters at the CSS orbit. The ground station LTFS is located in Wuhan, China, and its gravitational potential can be determined by leveling at the precision of centimeter level or better. Suppose $\alpha = 0$, and then we can calculate the true GRS value (model value) based on the GRT.

The next step is considering various error sources and simulating the observation values for a real case. For example, one of the primary error sources in the GRS test is clock instability. In our experiment, the stability of the on-board clock is set as $2 \times 10^{-15}/\sqrt{\tau}$ [15], the same stability as the one designed by CSS mission. The stability of the ground clock is supposed to be better. Various groups in the world have generated optical clocks with stabilities better than $1 \times 10^{-15}/\sqrt{\tau}$ [55,56]. As planned, the ground station will be equipped with the optical clock whose stability reaches $1 \times 10^{-15}/\sqrt{\tau}$. Table III shows relevant

TABLE III. Error sources and their magnitudes in the simulation experiments.

Error sources	Magnitudes
On-board clock stability	$2.0 \times 10^{-15}/\sqrt{\tau}$
Ground clock stability	$1.0 \times 10^{-15}/\sqrt{\tau}$
Troposphere influence residual	5% of the tropospheric frequency shift after combination ^a
Ionosphere influence residual	10% of the ionospheric frequency shift after combination ^a
Position accuracy of the CSS	± 0.1 m
Velocity accuracy of the CSS	$\pm 1.0 \times 10^{-3}$ m/s
Gravitational potential model accuracy	± 0.3 m ² /s ² (CSS), ± 0.5 m ² /s ² (ground)
Tide influence residual	0.1 m ² /s ²

^aCombination of up and down frequency signals, expressed as Eq. (2).

errors in our simulations. The accuracies of the tropospheric and ionospheric models reach 5% [28] and 10% [45,57], respectively. The position and velocity accuracy are set as the design values 10 cm and 1 mm/s, respectively [15]. The accuracies of geopotentials at the CSS and ground station are $0.3 \text{ m}^2/\text{s}^2$ and $0.5 \text{ m}^2/\text{s}^2$, respectively [53]. The tide model may correct the tide influence at $0.1 \text{ m}^2/\text{s}^2$ level [29,53].

The clock noises are classified as five different types of stochastic noises [58]. We analyzed the ratios of the five kinds of noises to the clock signals and restored the clock signals according to the different ratios. We set the stabilities of the ground clock and on-board clock as $1.0 \times 10^{-15}/\sqrt{\tau}$ and $2.0 \times 10^{-15}/\sqrt{\tau}$ [15], respectively (see Table III). Then we use a python library, Allantools (<https://github.com/aewallin/allantools>), to generate the series of clock frequency errors based on the characteristics of atomic clocks. Their total Allan deviations [58] are depicted in Fig. 5. The simulation results show the CSS clock stability reaches about 8×10^{-18} one day, and the ground clock performance is better than the CSS clock.

Another important influence factor is the frequency shift caused by the atmosphere. The meteorological elements of the ground station are downloaded from the CDDIS. The signal's tropospheric frequency shift is estimated based on the VMF. The ionospheric frequency shift can be calculated according to the model mentioned in Sec. III. The precision of the atmosphere model is regarded as residual errors and added to the frequency shift observation. Other error sources, such as the orbit error of CSS, the EGM2008 error,

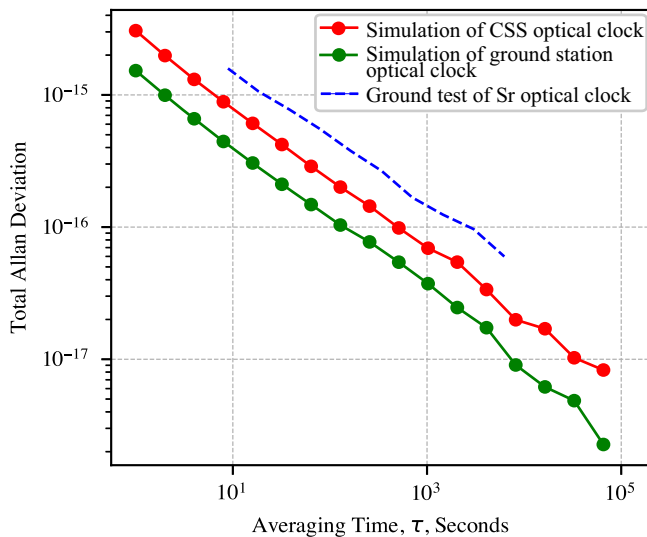


FIG. 5. The total Allan deviation of optical clocks' frequency signals. The red and green lines are the simulation clock error data for the CSS and ground station optical clock, and the stabilities reach $2.0 \times 10^{-15}/\sqrt{\tau}$ (τ in second) and $1.0 \times 10^{-15}/\sqrt{\tau}$, respectively. The blue dash line is ground test data of the Sr optical lattice clock. The test data starts at 8 s, and the stability reaches the magnitude of 5×10^{-17} after 4096 s (the data come from [59]).

and tidal correction residual, are also considered. Each of them is simulated as Gaussian errors plus a randomly set systematic offset. The magnitudes of error sources are listed in Table III.

Once the simulated observation frequency values are obtained, they are compared with the true frequency shift values and part of the offset between them (a short period lasts for about 5 minutes) is depicted in Fig. 6. From Fig. 6, the c^{-3} (mainly Shapiro effect) frequency shift residuals are the least influenced compared to other effects. The ionospheric frequency shift deviations (in absolute values, same sense hereafter) are less than 10^{-19} . The tropospheric frequency shift deviations are about $10^{-16} \sim 10^{-19}$, and the first-order and second-order Doppler frequency shift deviations are about 10^{-17} and 10^{-16} , respectively. The gravity frequency shift deviation remains at about 10^{-18} . We can see that the most prominent offset component comes from the clock error. The influence of ionosphere frequency shift shows apparent fluctuation because the total electron content distribution varies at different latitudes, and the extent of path discrepancy of uplink and downlink signals also varies at different elevation angles.

There are four sections (periods) in which the simulated observation data are available (see the solid black line in Fig. 4) during the one-day experiment. The result of the one-day experiment is $(0.17 \pm 3.05) \times 10^{-6}$, where 0.17×10^{-6} is the mean offset between the true value and the experiment result and $\pm 3.05 \times 10^{-6}$ is the uncertainty (STD). The offset of α reflects the precision of the GRS test experiment. However, the result of only one-day simulation experiment might be influenced by accidental factors. The observations are independent when the CSS passes the ground station. Therefore, we repeated the above

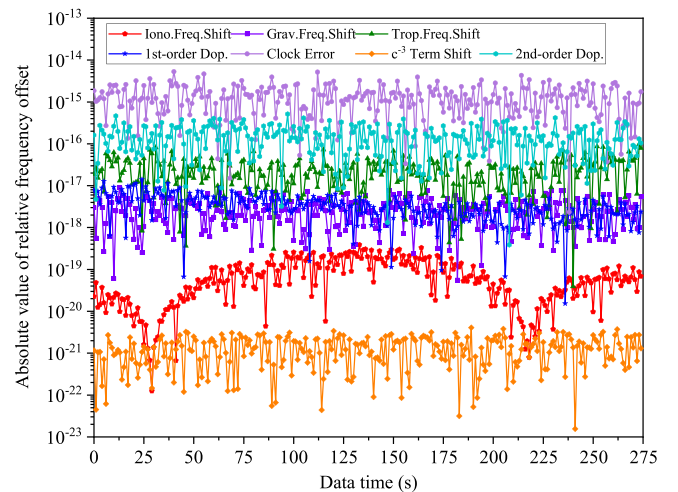


FIG. 6. Absolute value of relative frequency offset between theoretical predictions and simulated observations of a frequency shift during one slot period (around 5 min, from June 01, 09:34:18 to June 01, 09:38:52). The main error influence factors are denoted in different colors, marked in the upper legend corner.

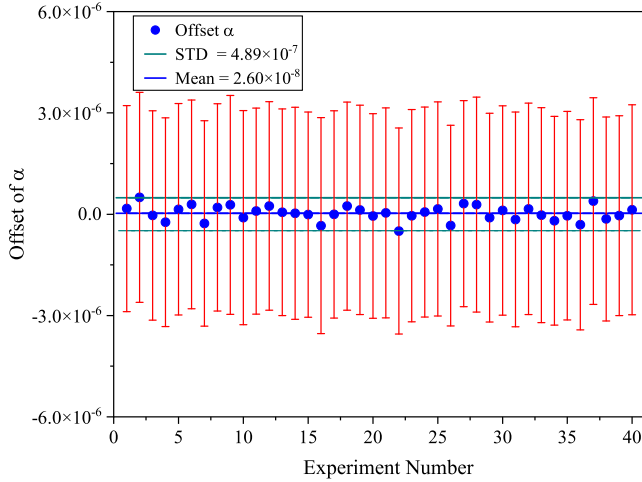


FIG. 7. The results of everyday simulation experiments of 40 independent days. The blue dots and red lines are the mean values and STD of everyday observation.

experiment 40 times for the same day under different random seeds of errors generation to estimate the precision of the GRS test, and the results of α offset of 40 days experiments are depicted in Fig. 7. The blue dots are the average values of daily simulation experiments. The weighted mean value of offset α for 40-day observations is 2.6×10^{-8} . The red vertical bars are the STD calculated each day. Everyday STD is approximately $\pm 3 \times 10^{-6}$. Here we use the weighted mean standard deviation formula $\delta = \sqrt{\sum_1^n \delta_i^2 w_i^2 / \sum_1^n w_i}$ to calculate the STD for 40-day, where n is the number of days, δ is the STD for n days and δ_i is i -day STD, w_i is the weight of i -day observation. Then the standard deviation of 40-day observations can be calculated and the value is 4.89×10^{-7} .

V. CONCLUSION

Based on the uplink and downlink frequency signals in free space between the CSS and a ground station, we

established a formulation for determining the gravitational potential difference between the CSS and the ground station. With this formulation, simulation results have shown that the GRS could be tested at around 5×10^{-7} , at least 2 orders of magnitude higher than the presently highest accuracy level. In addition, the proposed formulation in this study could be a new approach, applied to determining the geopotential difference between arbitrary two ground stations. In contrast, the conventional approach is gravimetry plus leveling [60], which is laborious and less efficient [61]. Suppose two ground stations equipped with optical clocks with the stability of 1×10^{-18} can simultaneously observe the frequency signals from CSS, the accuracy of determining the geopotential difference between the two ground stations could achieve a level of $0.14 \text{ m}^2/\text{s}^2$, because subtraction of the observation between CSS and one station and that between CSS and another station will cancel the common error sources stemming from CSS. With the rapid development of time-frequency science, the optical-atomic clocks with unprecedented accuracy and stability have been generated [55,62–66]. It dramatically expands the clocks application scopes in various branches. Besides its application in geopotential determination, this formulation can also be applied in height propagation between two datum stations separated by oceans, unifying the vertical height systems around the world.

ACKNOWLEDGMENTS

We would like to express our sincere thanks to the two anonymous reviewers for their valuable comments and suggestions, which greatly improved the manuscript. This study is supported by the National Natural Science Foundation of China (NSFC) (Grants No. 42030105, No. 41721003, No. 42274011), Space Station Project (Grant No. 2020-228), and Natural Science Foundation of Hubei Province (Grant No. 2019CFB611).

[1] R. F. C. Vessot and M. W. Levine, *Gen. Relativ. Gravit.* **10**, 181 (1979).
 [2] M. Takamoto, I. Ushijima, N. Ohmae, T. Yahagi, K. Kokado, H. Shinkai, and H. Katori, *Nat. Photonics* **14**, 411 (2020).
 [3] R. F. C. Vessot, M. W. Levine, E. M. Mattison, E. L. Blomberg, T. E. Hoffman, G. U. Nystrom, B. F. Farrell, R. Decher, P. B. Eby, C. R. Baugher, J. W. Watts, D. L. Teuber, and F. D. Wills, *Phys. Rev. Lett.* **45**, 2081 (1980).
 [4] J. Kouba, *GPS Solut.* **25**, 1 (2021).

[5] P. Delva, N. Puchades, E. Schönemann, F. Dilssner, C. Courde, S. Bertone, F. Gonzalez, A. Hees, C. Le Poncin-Lafitte, F. Meynadier, R. Prieto-Cerdeira, B. Sohet, J. Ventura-Traveset, and P. Wolf, *Phys. Rev. Lett.* **121**, 231101 (2018).
 [6] S. Herrmann, F. Finke, M. Lulf, O. Kichakova, D. Puetzfeld, D. Knickmann, M. List, B. Rievers, G. Giorgi, C. Günther, H. Dittus, R. Prieto-Cerdeira, F. Dilssner, F. Gonzalez, E. Schonemann, J. Ventura-Traveset, and C. Lammerzähl, *Phys. Rev. Lett.* **121**, 231102 (2018).

- [7] L. Cacciapuoti and C. Salomon, *J. Phys. Conf. Ser.* **327**, 012049 (2011).
- [8] F. Meynadier, P. Delva, C. le Poncin-Lafitte, C. Guerlin, and P. Wolf, *Classical Quantum Gravity* **35**, 035018 (2018).
- [9] L. Blanchet, C. Salomon, P. Teysandier, and P. Wolf, *Astron. Astrophys.* **370**, 320 (2001).
- [10] B. Linet and P. Teysandier, *Phys. Rev. D* **66**, 024045 (2002).
- [11] X. Sun, W.-B. Shen, Z. Shen, C. Cai, W. Xu, and P. Zhang, *Eur. Phys. J. C* **81**, 1 (2021).
- [12] Z. Shen, W.-B. Shen, T. Zhang, L. He, Z. Cai, X. Tian, and P. Zhang, *Adv. Space Res.* **68**, 2776 (2021).
- [13] Y.M. Guo, in *The 12th China Satellite Navigation Conference, CSNC 2021* (CSNC, Nanchang, China, 2021).
- [14] W.B. Wang, in *The 12th China Satellite Navigation Conference, CSNC 2021* (CSNC, Nanchang, China, 2021).
- [15] *China Space Station Science Experiment Resource Manual*, China Manned Space Engineering Office (2019), www.csu.cas.cn/gb/201905/P020190507639578655422.pdf.
- [16] S. Gao, Summary report of preliminary sample development of high precision time-frequency system, Technical Report, Chinese Academy of Sciences National Time Service Center, 2022.
- [17] J. Wang and L. Liu, Summary report of preliminary sample development of high precision time-frequency system, Technical Report, Chinese Academy of Sciences Shanghai Institute of Technical Physics and National Time Service Center, 2022.
- [18] L. Duchayne, Transfert de temps de haute performance: Le lien micro-onde de la mission ACES, Ph.D. thesis, Observatoire de Paris, 2008.
- [19] C. Anderson, S. Krishnamoorthy, C. Ranson, T. Lemon, W. Newhall, T. Kummert, and J. Reed, in *IEEE SoutheastCon, 2004. Proceedings* (IEEE, Greensboro, North Carolina, 2004), pp. 110–114, [10.1109/SECON.2004.1287906](https://doi.org/10.1109/SECON.2004.1287906).
- [20] S. Chen, M. Beach, and J. McGeehan, *Electron. Lett.* **34**, 147 (1998).
- [21] Y.-T. Yang, N. Chen, and C.-H. Zhu, in *3rd International Conference on Wireless Communication and Sensor Networks (WCSN 2016)* (Atlantis Press, Wuhan, China, 2016), pp. 31–36, [10.2991/icwdsn-16.2017.8](https://doi.org/10.2991/icwdsn-16.2017.8).
- [22] A. G. Longley, *Prediction of Tropospheric Radio Transmission Loss Over Irregular Terrain: A Computer Method-1968* (Institute for Telecommunication Sciences, Boulder, Colorado, 1968), Vol. 67.
- [23] S. Kasampalis, P. I. Lazaridis, Z. D. Zaharis, A. Bizopoulos, L. Paunovska, S. Zettas, I. A. Glover, D. Drogoudis, and J. Cosmas, in *2015 IEEE International Symposium on Broadband Multimedia Systems and Broadcasting* (IEEE, Ghent, Belgium, 2015), pp. 1–5, [10.1109/BMSB.2015.7177272](https://doi.org/10.1109/BMSB.2015.7177272).
- [24] M. Duarte, C. Dick, and A. Sabharwal, *IEEE Trans. Wireless Commun.* **11**, 4296 (2012).
- [25] D. Bharadia, E. McMillin, and S. Katti, in *Proceedings of the ACM SIGCOMM 2013 Conference on SIGCOMM* (Association for Computing Machinery, New York, USA, 2013), pp. 375–386, [10.1145/2486001.2486033](https://doi.org/10.1145/2486001.2486033).
- [26] J. Tamminen, M. Turunen, D. Korpi, T. Huusari, Y.-S. Choi, S. Talwar, and M. Valkama, in *2016 24th European Signal Processing Conference (EUSIPCO)* (IEEE, Budapest, Hungary, 2016), pp. 783–787, [10.1109/EUSIPCO.2016.776035](https://doi.org/10.1109/EUSIPCO.2016.776035).
- [27] X. Han, Research and implementation of digital self-interference suppression technology for aerospace tracking telemetering and command full-duplex system, Ph.D. thesis, University of electronic science and technology of China, 2021.
- [28] M. M. Hoque and N. Jakowski, *Global Navig. Satell. Syst.* **10**, 30090 (2012).
- [29] G. Petit and B. Luzum, *IERS Conventions* (2010), Technical Report, 2010.
- [30] T. Hartmann and H.-G. Wenzel, *Geophys. Res. Lett.* **22**, 3553 (1995).
- [31] H.-G. Wenzel, *Tidal Phenomena* (Springer, Berlin, Heidelberg, 1997), Vol. 9, [10.1007/BFb0011455](https://doi.org/10.1007/BFb0011455).
- [32] B. Hoffmann, *Phys. Rev.* **121**, 337 (1961).
- [33] D. Kleppner, R. F. C. Vessot, and N. F. Ramsey, *Astrophys. Space Sci.* **6**, 13 (1970).
- [34] J. A. Barnes, A. R. Chi, L. S. Cutler, D. J. Healey, D. B. Leeson, T. E. McGunigal, J. A. Mullen, W. L. Smith, R. L. Sydner, R. F. C. Vessot, and G. M. R. Winkler, *IEEE Trans. Instrum. Meas.* **IM-20**, 105 (1971).
- [35] W. J. H. Riley, in *IEEE International Frequency Control Symposium, Tampa, FL* (IEEE, Tampa, USA, 2003), Vol. 4.
- [36] D. Allan, *Proc. IEEE* **54**, 221 (1966).
- [37] P. Lesage and C. Audoin, *Radio Sci.* **14**, 521 (1979).
- [38] A. Siegman and R. Arrathoon, *Phys. Rev. Lett.* **20**, 901 (1968).
- [39] R. Vessot, M. Levine, and E. Mattison, Comparison of theoretical and observed hydrogen maser stability limitation due to thermal noise and the prospect for improvement by low-temperature operation, Technical Report, Harvard Coll Observatory Cambridge Mass Center for Astrophysics, 1977.
- [40] S. Namazov, V. Novikov, and I. Khmel’Nitskii, *Radiophys. Quantum Electron.* **18**, 345 (1975).
- [41] J. Bennett, *Aust. J. Phys.* **21**, 259 (1968).
- [42] Z. Shen, W.-B. Shen, and S. Zhang, *Geophys. J. Int.* **206**, 1162 (2016).
- [43] M. M. Hoque and N. Jakowski, *J. Geod.* **81**, 259 (2007).
- [44] J. M. Rüeger, in *Proceedings of the FIG XXII International Congress, Washington, DC, USA* (FIG XXII International Congress, Washington, DC, USA, 2002), Vol. 113.
- [45] J. Saastamoinen, *The Use of Artificial Satellites for Geodesy* (American Geophysical Union (AGU), 1972).
- [46] J. Böhm and H. Schuh, in *16th EVGA Working Meeting* (2003), [10.1029/2003GL018984](https://doi.org/10.1029/2003GL018984).
- [47] L. Weiping, Q. Hongxing, and D. Qi, in *2012 IEEE International Conference on Information and Automation* (IEEE, Shenyang, China, 2012), pp. 811–813, [10.1109/ICInfA.2012.6246892](https://doi.org/10.1109/ICInfA.2012.6246892).
- [48] <http://www.celestrak.com/NORAD/elements/>.
- [49] <https://cdsis.nasa.gov/archive/gnss/data/daily/>.
- [50] D. Bilitza, K. Rawer, L. Bossy, and T. Gulyaeva, *Adv. Space Res.* **13**, 15 (1993).
- [51] J. Baerenzung, M. Holschneider, J. Wicht, V. Lesur, and S. Sanchez, *Earth Planets Space* **72**, 1 (2020).
- [52] <https://github.com/joernc/tidal-potential>.

- [53] N. K. Pavlis, S. A. Holmes, S. C. Kenyon, and J. K. Factor, in *AGU Fall Meeting Abstracts* (2008), Vol. 2008, pp. G22A–01.
- [54] N. K. Pavlis, S. A. Holmes, S. C. Kenyon, and J. K. Factor, *J. Geophys. Res.* **117**, 1 (2012).
- [55] S. M. Brewer, J.-S. Chen, A. M. Hankin, E. R. Clements, C.-W. Chou, D. J. Wineland, D. B. Hume, and D. R. Leibbrandt, *Phys. Rev. Lett.* **123**, 033201 (2019).
- [56] T. Bothwell, C. J. Kennedy, A. Aeppli, D. Kedar, J. M. Robinson, E. Oelker, A. Staron, and J. Ye, *Nature (London)* **602**, 420 (2022).
- [57] D. Landskron and J. Böhm, *J. Geod.* **92**, 349 (2018).
- [58] D. W. Allan, M. A. Weiss, and J. L. Jespersen, in *Proceedings of the 45th Annual Symposium on Frequency Control 1991* (IEEE, 1991), pp. 667–678.
- [59] F. Guo, W. Tan, C.-h. Zhou, J. Xia, Y.-x. Chen, T. Liang, Q. Liu, Y. Liu, D.-j. He, Y.-z. Zhou *et al.*, *AIP Adv.* **11**, 125116 (2021).
- [60] W. A. Heiskanen and H. Moritz, *Physical Geodesy (Book on Physical Geodesy Covering Potential Theory, Gravity Fields, Gravimetric and Astrogeodetic Methods, Statistical Analysis, etc)* (W. H. Freeman and Company, San Francisco, 1967).
- [61] Z. Shen, W.-B. Shen, and S. Zhang, [arXiv:2008.05868](https://arxiv.org/abs/2008.05868).
- [62] T. L. Nicholson, S. L. Campbell, R. B. Hutson, G. E. Marti, B. J. Bloom, R. L. McNally, W. Zhang, M. D. Barrett, M. S. Safronova, G. F. Strouse *et al.*, *Nat. Commun.* **6**, 1 (2015).
- [63] N. Huntemann, C. Sanner, B. Lipphardt, C. Tamm, and E. Peik, *Phys. Rev. Lett.* **116**, 063001 (2016).
- [64] W. F. McGrew, X. Zhang, R. J. Fasano, S. A. Schäffer, K. Beloy, D. Nicolodi, R. C. Brown, N. Hinkley, G. Milani, M. Schioppo, T. H. Yoon, and A. D. Ludlow, *Nature (London)* **564**, 87 (2018).
- [65] E. Oelker, R. B. Hutson, C. J. Kennedy, L. Sonderhouse, T. Bothwell, A. Goban, D. Kedar, C. Sanner, J. M. Robinson, G. E. Marti *et al.*, *Nat. Photonics* **13**, 714 (2019).
- [66] T. Nakamura, J. Davila-Rodriguez, H. Leopardi, J. A. Sherman, T. M. Fortier, X. Xie, J. C. Campbell, W. F. McGrew, X. Zhang, Y. S. Hassan *et al.*, *Science* **368**, 889 (2020).

Correction: An affiliation for the sixth author was missing at the time of publication and has been inserted as the fifth affiliation.